Journal of Sound and Vibration (2002) **257**(3), 503–525
doi:10.1006/jsvi.5050, available online at http://www.idealibrary.com on IDEAL®

VIBRATION AND STABILITY CONTROL OF SMART COMPOSITE ROTATING SHAFT VIA STRUCTURAL TAILORING AND PIEZOELECTRIC STRAIN ACTUATION

O. SONG

Mechanical Engineering Department, Chungnam National University, Taejon, 305-764, *Korea*

L. LIBRESCU

Engineering Science and Mechanics Department, Virginia Polytechnic Institute and State University, Blacksburg, VA 24061-0219, *U.S.A. E-mail*: *librescu@vt.edu*

AND

N-H. JEONG

Mechanical Engineering Department, Chungnam National University, Taejon, 305-764, *Korea*

(*Received* 11 *September* 2001, *and in final form* 11 *January* 2002)

A dual approach based on both structural tailoring and piezoelectric strain actuation, aimed at controlling the free vibration and stability of a spinning circular shaft subjected to axial forces is presented. Due to the involvement in these structural systems of gyroscopic forces and, consequently, of the possible occurrence of divergence and flutter instabilities, the dual control methodology shows a high degree of efficiency toward postponement of the occurrence of these instabilities. The structural model of the shaft as considered in this paper is based on an advanced thin-walled beam that includes the effects of transverse shear, anisotropy of constituent materials, rotatory inertias, etc. The displayed results reveal the synergistic implications of the application of this dual technology toward the enhancement of the dynamic response characteristics and expansion of the domain of stability of these systems.

© 2002 Elsevier Science Ltd. All rights reserved.

1. INTRODUCTION

The rotating flexible shaft is one of the most important structural elements employed for power transmission in aeropropulsion systems, helicopter drive applications, industrial machines such as steam and gas turbines, turbogenerators and precision manufacturing. In each of these cases, the reliability of the machinery depends on the stability of the rotating shaft elements. Moreover, in order to enhance the vibrational behavior of the flexible shaft and reduce its weight, advanced structural models are required.

To this end, the integration of composite material systems is likely to contribute to the increase in performance of these devices. In addition to their superior strength/weight and stiffness/weight ratios as compared to their metallic counterparts, the directionality property featured by fiber composite material systems can be used to tailor the stiffness properties of the flexible shaft. In such a way, new exotic elastic couplings, not featured by the standard metallic shaft counterpart, having beneficial implications upon their response

0022-460X/02/$35.00 © 2002 Elsevier Science Ltd. All rights reserved.

can be generated. However, the tailoring technique is passive in its nature, in the sense that once implemented, the structure is not able to respond in a way that avoids the occurrence of resonance and of any instability that can jeopardize its operational life.

As a complementary option, the control via the implementation of the adaptive material technology can be applied.

In a structure with adaptive capabilities its dynamic response characteristics can be controlled in a known and predictable manner and, as a result, one can avoid the occurrence of the structural resonance and of any static and dynamic instability.

The adaptive capability can be achieved through both the converse and direct piezoelectric effects. In this sense, the capability generated by the former effect, referred to as the actuating one, consists of the generation of localized strains in response to an applied voltage, whereas the sensing capability, obtained via the direct piezoelectric effect, consists of the generation of a charge/voltage as a result of the application of a force.

In this paper, a study of the enhancement of the vibrational response and of stability of spinning flexible shaft via the implementation of both techniques, namely, of the *adaptive capability* and of the *structural tailoring* will be carried out.

Implementation of a control law relating the applied electric field with one of the kinematical response quantities of the host structure according to a prescribed functional relationship, results in a dynamic boundary-value problem. Its solution yields the *closed-loop dynamic response* characteristics.

Although belonging to the class of conservative systems, due to the involvement of gyroscopic forces, the rotating shaft can feature, in some conditions, both the divergence and flutter instabilities. Having in view that the flutter instability is a catastrophic failure, the postponement of its occurrence constitutes a problem of a vital importance toward a prolonged and safe use of these devices.

In the present paper, the flexible rotating shaft is modelled as a thin-walled composite beam of circular cross-section, incorporating smart materials technology, and in this sense, the piezoelectric materials that can play the role of sensors and actuators will be used.

In spite of the great importance of this topic, to the best of the authors' knowledge, the literature devoted to the modelling, and stability of spinning shaft considered as a thin-walled beam is very scanty. The reader is referred to references [1, 2] where ample references to the pertinent literature addressing these issues are supplied.

Moreover, an appraisal of the performance of the structural model used in this paper, in the context of the available experimental and analytical results was provided in reference [3].

2. CO-ORDINATE SYSTEMS, BASIC ASSUMPTIONS

The case of a straight untwisted flexible thin-walled beam of length L spinning along its longitudinal z-axis at a constant rate Ω and subjected to a longitudinal compressive dead force P is considered (see Figure 1). Two sets of co-ordinates, an inertial one $OXYZ$, and a body attached rotating frame of reference $Oxyz$ with the common origin O, located in the geometric center (coinciding with the elastic center of the beam), are considered. It is supposed that at $t = 0$, the axes of the two systems coincide while, in the undeformed configuration, the body-fixed and inertial co-ordinates Oz and OZ coincide at any time t. Associated with the rotating and absolute co-ordinate systems (x, y, z) and (X, Y, Z), one define the unit vectors $(\mathbf{i}, \mathbf{j}, \mathbf{k})$ and $(\mathbf{I}, \mathbf{J}, \mathbf{K})$ respectively. In addition to the previously defined co-ordinate systems, a local one, (n, s, z), is considered. In the light of the

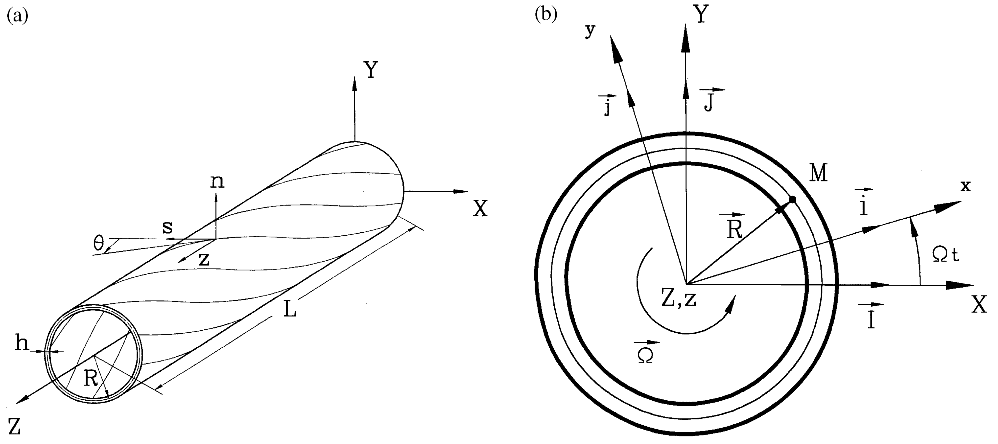

Figure 1. Geometry of composite thin-walled beam of circular cross-section featuring CUS configuration; (a) global view; (b) cross-section view.

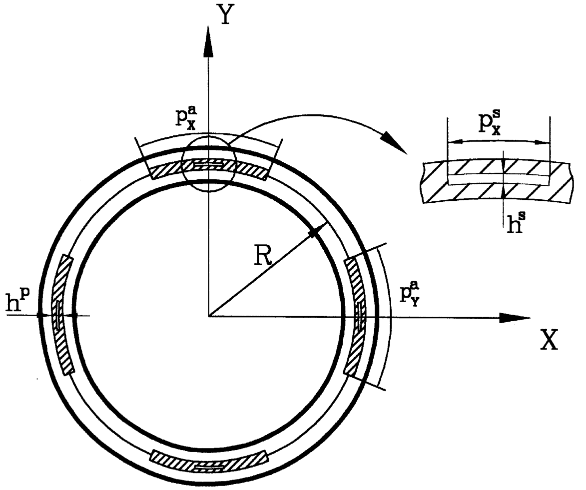

Figure 2. Piezoactuator and piezosensor patch distributions.

stipulated assumptions one can represent the spin rate vector as $\boldsymbol{\Omega} = \Omega\mathbf{k}$ ($\equiv \Omega\mathbf{K}$) with $\dot{\Omega} = 0$.

In this context, the case of a single-cell thin-walled beam of circular cross-sectional shape is considered. Toward its modelling the following assumptions are adopted: (1) the original cross-section of the beam is preserved, (2) transverse shear effects are incorporated, (3) the constituent material of the structure features anisotropic properties, and, in this context, a special lay-up inducing flapping–lagging coupling is implemented, and finally, (4) the piezoactuators are spread over the entire beam span on the top and bottom faces and on the left- and right-hand sides of the master structure as indicated in Figure 2, and are *activated out of phase*.

3. KINEMATICS

In light of the previously mentioned assumptions and in order to reduce the 3-D elasticity problem to an equivalent 1-D one, the components of the displacement vector are represented as (see, e.g., references [1, 4, 5])

$$u(x,y,z;t) = u_0(z;t) - y\phi(z;t), \quad v(x,y,z;t) = v_0(z;t) + x\phi(z;t),$$

$$w(x,y,z;t) = w_0(z;t) + \theta_x(z;t)\left[y(s) - n\frac{\mathrm{d}x}{\mathrm{d}s}\right] + \theta_y(z;t)\left[x(s) + n\frac{\mathrm{d}y}{\mathrm{d}s}\right] - \phi'(z;t)[F_\omega(s) + na(s)]. \qquad \text{(1a–c)}$$

In these equations $u_0(z;t)$, $v_0(z;t)$, $w_0(z;t)$ denote the rigid-body translations along the x-, y- and z-axis, while $\phi(z;t)$, $\theta_x(z;t)$ and $\theta_y(z,t)$ denote the twist about the z-axis and rotations about the x- and y-axis, respectively. The expressions of θ_x and θ_y as well as of the geometric quantity $a(s)$ are

$$\theta_x(z;t) = \gamma_{yz}(z;t) - v_0'(z;t), \qquad \theta_y(z;t) = \gamma_{xz}(z;t) - u_0'(z;t), \qquad \text{(2a–c)}$$

$$a(s) = -y(s)\frac{\mathrm{d}y}{\mathrm{d}s} - x(s)\frac{\mathrm{d}x}{\mathrm{d}s}.$$

In equations (1), $F_\omega(s)$ and $na(s)$ play the role of primary and secondary warping functions respectively. For their definition see e.g., references [1, 4]. However, for thin-walled beams of circular cross-sections, having in view that

$$x = -R\sin(s/R), \qquad y = R\cos(s/R) \quad \text{and} \quad r_n(s) = R, \qquad \text{(2d–f)}$$

where R is the beam radius of the mid-line cross-section, it can readily be proven that both warping quantities exactly vanish, i.e.,

$$F_\omega(s) = 0 \quad \text{and} \quad a(s) = 0. \qquad \text{(2g, h)}$$

It is also seen that in the absence of transverse shear effects,

$$\theta_x(z;t) = -v_0'(z;t), \qquad \theta_y(z;t) = -u_0'(z;t). \qquad (3)$$

In these equations, as well as in the forthcoming ones, the primes denote differentiation with respect to the longitudinal z-co-ordinate. The position vector of a generic point $M(x,y,z)$ belonging to the deformed structure is

$$\mathbf{R}(x,y,z;t) = (x+u)\mathbf{i} + (y+v)\mathbf{j} + (z+w)\mathbf{k}, \qquad (4)$$

where x, y and z are the Cartesian co-ordinates of the points of the continuum in its undeformed state. Recalling that the spin rate was assumed to be constant, and using the expressions for the time derivatives of unit vectors, the velocity and acceleration of a generic point are

$$\dot{\mathbf{R}} = [\dot{u} - \Omega(y+v)]\mathbf{i} + [\dot{v} + \Omega(x+u)]\mathbf{j} + \dot{w}\mathbf{k}, \qquad \text{(5a, b)}$$

$$\ddot{\mathbf{R}} = [\ddot{u} - 2\Omega\dot{v} - (x+u)\Omega^2]\mathbf{i} + [\ddot{v} + 2\Omega\dot{u} - (y+v)\Omega^2]\mathbf{j} + \ddot{w}\mathbf{k}.$$

In these equations the superposed dots denote derivatives with respect to the time t.

4. GOVERNING SYSTEM

Toward the goal of deriving the equations of motion of spinning beams and the associated boundary conditions, Hamilton's principle was used. In addition, in order to induce the elastic couplings between flapwise bending and chordwise bending, a special ply-angle distribution resulting in a *circumferentially uniform stiffness* (CUS) configuration is implemented (see references [6, 7]). This configuration is achieved by skewing angle plies with respect to the longitudinal beam axis according to the law $\theta(y) = \theta(-y)$, and $\theta(x) = \theta(-x)$, where θ denotes the ply-angle measured from the positive s-axis toward the positive z-co-ordinate.

In this case, Hamilton's principle provides the equations of motion and the boundary conditions involving this type of coupling and incorporating transverse shear effects. Representation of the equations of motion in terms of displacement quantities results in the following *governing system*:

$$\begin{aligned}
\delta u_0&:\quad a_{43}\theta_x'' + a_{44}(u_0'' + \theta_y') - Pu_0'' = b_1\ddot{u}_0 - 2b_1\Omega\dot{v}_0 - b_1u_0\Omega^2,\\
\delta v_0&:\quad a_{52}\theta_y'' + a_{55}(v_0'' + \theta_x') - Pv_0'' = b_1\ddot{v}_0 + 2b_1\Omega\dot{u}_0 - b_1v_0\Omega^2,\\
\delta\theta_y&:\quad a_{22}\theta_y'' + a_{25}(v_0'' + \theta_x') - a_{44}(u_0' + \theta_y) - a_{43}\theta_x' = \underline{(b_5 + b_{15})\ddot{\theta}_y},\\
\delta\theta_x&:\quad a_{33}\theta_x'' + a_{34}(u_0'' + \theta_y') - a_{55}(v_0' + \theta_x) - a_{52}\theta_y' = \underline{(b_4 + b_{14})\ddot{\theta}_x}.
\end{aligned} \tag{6}$$

For cantilevered beams, the boundary conditions at the beam root are entirely kinematic and at the tip, entirely static.

As a result, at $z = 0$ these are

$$u_0 = \underset{\sim}{u}_0, \qquad v_0 = \underset{\sim}{v}_0, \qquad \theta_y = \underset{\sim}{\theta}_y \quad \text{and} \quad \theta_x = \underset{\sim}{\theta}_x, \tag{7a}$$

while at $z = L$, these are

$$\delta u_0 : Q_x = \underset{\sim}{Q}_x, \quad \delta v_0 : Q_y = \underset{\sim}{Q}_y, \quad \delta\theta_y : M_y = \underset{\sim}{M}_y, \quad \delta\theta_x\!: \quad M_x = \underset{\sim}{M}_x. \tag{7b}$$

Herein $Q_x(z;t)$ and $Q_y(z;t)$ denote the shear forces in the x and y directions, $M_x(z;t)$ and $M_y(z;t)$ denote the moments about the x- and y-axis, respectively, P is the constant axial force, positive in compression, whereas the terms underscored by the interrupted and solid lines are associated with Coriolis and rotatory inertia effects, respectively. In the case of the piezoactuators spread over the entire span of the beam, symmetrically located (see Figure 2) and activated out of phase, the piezoelectrically induced bending moments $\hat{M}_x$ and $\hat{M}_y$ are generated at the beam tip (see, e.g., references [8, 9]). These bending moments appear in the boundary conditions at the beam tip and as a result, the control is accomplished via the piezoelectrically induced boundary bending moments.

Using the constitutive equations for the shear forces and moments (see references [1, 3, 4]), the static version of boundary conditions at the beam tip in terms of displacement quantities is

$$\begin{aligned}
\delta u_0&:\quad a_{43}\theta_x' + a_{44}(u_0' + \theta_y) - Pu_0' = 0,\\
\delta v_0&:\quad a_{52}\theta_y' + a_{55}(v_0' + \theta_x) - Pv_0' = 0,\\
\delta\theta_y&:\quad a_{22}\theta_y' + a_{25}(v_0' + \theta_x) + \hat{M}_y = 0,\\
\delta\theta_x&:\quad a_{33}\theta_x' + a_{34}(u_0' + \theta_y) + \hat{M}_x = 0.
\end{aligned} \tag{8}$$

The coefficients $a_{ij} = a_{ji}$ and b_i appearing in these equations denote stiffness and reduced mass terms, respectively. Their expressions are supplied in Appendix A. Equations (6) and (8) reveal that in the context of the above considered ply-angle configuration, in addition to the already mentioned elastic couplings that are materialized by the stiffnesses a_{25} $(= a_{52})$ and a_{34} $(= a_{43})$, the flapwise transverse shear is also coupled with chordwise bending and the chordwise transverse shear is coupled with flapwise bending. Moreover, the Coriolis acceleration terms induce a supplementary coupling between the flapwise and chordwise bendings.

Separately of the above-mentioned couplings, the extension–twist coupling is induced by the same ply-angle configuration. This type of coupling is important and implemented as such, e.g., in helicopter blades and tilt rotor aircraft. However, the present study is confined to the problem involving the flapwise–chordwise bending coupling only, and, as a result, the equations involving extension–twist coupling are not displayed here.

5. SPECIAL CASE: UNSHEARABLE BEAM MODEL

For this case, elimination from equations (6) and (8) of the quantities $a_{44}(u_0'' + \theta_y')$ and $a_{55}(v_0'' + \theta_x')$, the operation followed by consideration of equation (3) stating the absence of transverse shear results in the governing equations

$$\delta u_0\colon \quad a_{22}u_0'''' + Pu_0'' + b_1\ddot{u}_0 - \underline{(b_5 + b_{15})\ddot{u}_0''} - 2b_1\Omega\dot{v}_0 - b_1 u_0\Omega^2 = 0, \tag{9a}$$

$$\delta v_0\colon \quad a_{33}v_0'''' + Pv_0'' + b_1\ddot{v}_0 - \underline{(b_4 + b_{14})\ddot{v}_0''} - 2b_1\Omega\dot{u}_0 - b_1 v_0\Omega^2 = 0 \tag{9b}$$

and the boundary conditions. Their homogeneous counterpart is
at $z = 0$:

$$u_0 = v_0 = u_0' = v_0' = 0 \tag{10a-c}$$

and at $z = L$:

$$\delta u_0\colon \quad a_{22}u_0''' + Pu_0' - \underline{(b_5 + b_{15})\ddot{u}_0'} = 0, \tag{11a}$$

$$\delta v_0\colon \quad a_{33}v_0''' + Pv_0' - \underline{(b_4 + b_{14})\ddot{v}_0'} = 0, \tag{11b}$$

$$\delta u_0'\colon \quad a_{22}u_0'' = \hat{M}_y, \qquad \delta v_0'\colon \quad a_{33}v_0'' = \hat{M}_x. \tag{11c, d}$$

It should be remarked that the governing equations of shearable thin-walled beams (equations (6) and (8)), and their non-shear deformable counterparts, equations (9)–(11), exhibit the same order, namely eight, and as such, in both cases, four boundary conditions have to be prescribed at each end, $z = 0$, L, of the beam. Equations (9) reveal that in this special case, the coupling arises only via Coriolis acceleration effect. In its absence, both equations would be decoupled. It is also seen that in the case of the non-shearable beams, and in contrast to their shearable counterparts, the rotatory inertia terms appear also in the boundary conditions.

6. PIEZOACTUATORS AND THE CONTROL LAW

It is assumed that the master structure is composed of r layers while the actuator is composed of p piezoelectric layers. We stipulate that the actuators are distributed over the entire span of the beam, whereas along the circumferential and transverse directions, i.e., along the s and n directions, they are distributed according to the law

$$S_{(k)}(n) = \mathrm{H}(n - n_{(k^-)}) - \mathrm{H}(n - n_{(k^+)}), \quad S_{(k)}(s) = \mathrm{H}(s - s_{(k^-)}) - \mathrm{H}(s - s_{(k^+)}). \tag{12a, b}$$

Herein H denotes Heaviside's distribution, S is a spatial function that defines the distribution of actuators in the n and the s directions, and the subscript k identifies the affiliation of the respective quantity with the kth layer.

Assuming that the electric field vector $\mathscr{E}_i$ is represented by its component $\mathscr{E}_3$ in the n direction coinciding with the direction of polarization (referred to as thickness polarization), the boundary bending moment controls are expressed as

$$\hat{M}_x = \oint \sum_{k=1}^{p} \mathscr{E}_3^{(k)} \left(n_{(k+)} - n_{(k-)}\right) e_{31}^{(k)} S_{(k)}(s) \left[y\left(1 - \frac{\hat{A}_{12}}{\hat{A}_{11}}\right) + \frac{\mathrm{d}x}{\mathrm{d}s}\frac{\hat{B}_{12}}{\hat{A}_{11}}\right] \mathrm{d}s$$
$$- \frac{1}{2}\oint \left[\frac{\mathrm{d}x}{\mathrm{d}s} \sum_{k=1}^{p} \mathscr{E}_3^{(k)} \left(n^2_{(k+)} - n^2_{(k-)}\right) e_{31}^{(k)} S_{(k)}(s)\right] \mathrm{d}s, \tag{13a}$$

$$\hat{M}_y = \oint \sum_{k=1}^{p} \mathscr{E}_3^{(k)} \left(n_{(k+)} - n_{(k-)}\right) e_{31}^{(k)} S_{(k)}(s) \left[x\left(1 - \frac{\hat{A}_{12}}{\hat{A}_{11}}\right) + \frac{\mathrm{d}y}{\mathrm{d}s}\frac{\hat{B}_{12}}{\hat{A}_{11}}\right] \mathrm{d}s$$
$$+ \frac{1}{2}\oint \left[\frac{\mathrm{d}y}{\mathrm{d}s} \sum_{k=1}^{p} \mathscr{E}_3^{(k)} \left(n^2_{(k+)} - n^2_{(k-)}\right) e_{31}^{(k)} S_{(k)}(s)\right] \mathrm{d}s. \tag{13b}$$

Herein e_{31} is the piezoelectric constant; $\hat{A}_{ij}$ and $\hat{B}_{ij}$ are the standard local-stiffness quantities associated with the piezoactuators, while $\oint(\cdot)\,\mathrm{d}s$ denotes the integral around the circumference of the mid-line cross-section of the beam.

For $\mathscr{E}_3$ constant throughout the piezoactuator thickness, this implying $\mathscr{E}_3^{(k)} \equiv \mathscr{E}_3$, equations (13) can be expressed in condensed form as

$$\hat{M}_x = \mathscr{E}_3 \mathscr{M}_x, \qquad \hat{M}_y = \mathscr{E}_3 \mathscr{M}_y, \tag{14a, b}$$

where the meaning of $\mathscr{M}_x$ and $\mathscr{M}_y$ becomes evident by comparing equations (14) with equations (13).

Equations (13) and (14) reveal that the piezoelectrically induced bending moments are proportional to the applied electric field $\mathscr{E}_3$. Now, assuming that the piezoelectric elements are employed for the sensing operation, the electric displacement is

$$D_3 = e_{31} S_{zz} \tag{15}$$

and the sensor output voltage is expressed in the form

$$V_s(t) = \frac{q_s(t)}{C_p}, \tag{16}$$

where the electric charge $q_s(t)$ is

$$q_s(t) = \int_{A_2} D_3\,\mathrm{d}A_s = \int_{A_s} e_{31} S_{zz}\,\mathrm{d}A_s. \tag{17}$$

In these equations C_p and A_s denote the sensor's capacitance and piezoelectric patch area, respectively, while S_{zz} denotes the axial strain component. Assuming the sensor patches being located symmetrically on the opposite walls, i.e., on $y = \pm R$ and $x = \pm R$; the expression of S_{zz}, $V_s^x(t)$ and $V_s^y(t)$ are expressible as

$$V_s^x(t) = C_x^s \theta_x(L, t), \qquad V_s^y(t) = C_y^s \theta_y(L, t), \tag{18a, b}$$

where the expressions of C_y^s and C_x^s are not displayed here.

The feedback control law to be used here is referred to as *the proportional feedback control law*.

Within this control law, one postulates [10], that the actuating electric field is proportional to the sensor output voltage, which implies

$$\mathscr{E}_3^x(t) = K_p V_s^x(t)/h_a, \qquad \mathscr{E}_3^y(t) = K_p V_s^y(t)/h_a, \tag{19a, b}$$

where h_a is the thickness of the piezopatch, and K_p is the proportional feedback gain.

As a result, replacement of equations (19) considered in conjunction with substituting equations (18) into equations (14), yields the piezoelectrically induced bending moments expressed as

$$\hat{M}_y(L,t) = \frac{K_p C_{M_y^a}}{h_a}[C_y^s \theta_y(L,t)] = K_p C_{11}\theta_y(L,t), \tag{20a}$$

$$\hat{M}_x(L,t) = \frac{K_p C_{M_x^a}}{h_a}[C_x^s \theta_x(L,t)] = K_p C_{22}\theta_x(L,t). \tag{20b}$$

The results yielding the piezoelectrically induced bending moments, equations (20), reveal that these are obtained through the combination of both sensing and actuation functions.

Herein,

$$C_{M_y^a} = \sum_{k=1}^{r} e_{31}^{(k)}\left[\left(1-\frac{\hat{A}_{11}}{\hat{A}_{12}}\right)(n_{(k^+)}-n_{(k^-)}) + (n_{(k^+)}^2 - n_{(k^-)}^2) - 2\frac{\hat{B}_{12}}{\hat{A}_{11}}(n_{(k^+)}-n_{(k^-)})\right]p_2, \tag{21a}$$

$$C_{M_x^a} = \sum_{k=1}^{r} e_{31}^{(k)}\left[\left(1-\frac{\hat{A}_{11}}{\hat{A}_{12}}\right)(n_{(k^+)}-n_{(k^-)}) + (n_{(k^+)}^2 - n_{(k^-)}^2) - 2\frac{\hat{B}_{12}}{\hat{A}_{11}}(n_{(k^+)}-n_{(k^-)})\right]p_1, \tag{21b}$$

where p_1 and p_2 denote the lengths of the piezoactuators along the circumferential direction (see Figure 2), while r stands for the number of piezoactuator layers.

Concerning the proportional feedback gain, K_p, this will be used in dimensionless form as

$$\bar{K}_p = \frac{K_p L}{\hat{a}_{33} h_p}, \tag{22}$$

where $\hat{a}_{33}$ is the transverse bending stiffness corresponding to the ply-angle $\theta = 0$.

The eigenvalue problem involving the coupled governing equation (6) considered in conjunction with the boundary conditions (7) and (8), and the control law (20), yields the closed-loop eigenvalue problem related to the problem of spinning thin-walled beams.

7. THE DISCRETIZED GOVERNING EQUATIONS

In order to find an approximate solution to this intricate eigenproblem, assuming synchronous motions, the generalized displacements are represented in the form

$$(u_0(z,t), v_0(z,t), \theta_x(z,t), \theta_y(z,t)) = (U(z), V(z), X(z), Y(z))\mathrm{e}^{\mathrm{i}\omega t}, \tag{23a}$$

where ω is the complex eigenfrequency, while the spatial parts are represented as

$$(U(z), V(z), X(z), Y(z)) = \sum_{j=1}^{N} (a_j u_j(z), b_j v_j(z), c_j x_j(z), d_j y_j(z)), \tag{23b}$$

where $u_j(z), v_j(z), x_j(z)$ and $y_j(z)$ are trial functions which have to fulfill all the kinematic boundary conditions.

In the spirit of the extended Galerkin method [11] representations (23) are replaced in Hamilton's variational functional, where the indicated variations and the required integrations with respect to the spanwise z-co-ordinate and time t are carried out. In this way, the system of governing equations is cast in matrix form as

$$\delta\mathbf{B}^{\mathrm{T}}[-\omega^2\mathbf{M}_N + \mathrm{i}\omega\mathbf{G}_N + \mathbf{K}_N]\mathbf{B} = 0, \tag{24a}$$

where

$$\mathbf{B}^{\mathrm{T}} = [a_1, a_2, \ldots, a_N, b_1, b_2, \ldots, b_N, c_1, c_2, \ldots, c_N, d_1, d_2, \ldots, d_N] \tag{24b}$$

is a constant vector. Herein $\mathbf{M}_N, \mathbf{G}_N$ and $\mathbf{K}_N$ are $(2N \times 2N)$ matrices, $\mathbf{M}_N$ being the symmetric positive definite, $\mathbf{G}_N$ the skew symmetric and $\mathbf{K}_N$ the symmetric. $\mathbf{G}_N$ is due entirely to the gyroscopic effects. In the absence of the Coriolis effect, $\mathbf{G}_N$ would be immaterial. Since contributions from the external compressive load, centrifugal forces and piezoelectric control are included in $\mathbf{K}_N$; its positive definiteness, positive semidefiniteness or negative definiteness cannot be postulated *a priori*.

Equation (24a) provides the characteristic equation

$$\Delta_N(\omega, P, \Omega^2, \bar{K}_p) = \det[-\omega^2\mathbf{M}_N + \mathrm{i}\omega\mathbf{G}_N + \mathbf{K}_N] = 0, \tag{25}$$

where from ω can be obtained. If $\mathbf{K}_N$ is positive definite, and $\mathbf{G}_N \neq 0$, the characteristic polynomial resulting from the expansion of determinant (25) will be a function of ω^2. The system remains stable as long as all ω_k^2 are real and positive.

For a fixed compressive load, the minimum spin rate at which the whirl frequency ω_j becomes zero valued, corresponds to the critical spinning speed, denoted as Ω_{cr}. Conversely, for a fixed spin rate, the minimum compressive load for which one of the roots ω_j becomes zero, corresponds to the critical compressive load P_{cr}. The instability described above is of the divergence type. In general, the condition of divergence is obtained by taking $\omega = 0$ in equation (25), which yields the equation

$$\Delta_N(P, \Omega^2, \bar{K}_p) = 0. \tag{26}$$

Equation (26) supplies the divergence boundary of instability in the presence of the piezoelectric actuation. It is clearly seen that the divergence instability, being a static phenomenon, is the same for both the gyroscopic and non-gyroscopic systems. On the other hand, combinations of compressive load and spin rate yielding two eigenfrequencies to coalesce, constitutes a flutter condition. Increase of either of these two parameters beyond the value of the load or spin rate corresponding to the flutter boundary, results in complex conjugate eigenvalues, and correspondingly, to bending oscillations with exponentially increasing amplitudes. This clearly reveals that the occurrence of the flutter instability results in the catastrophic failure of the system. In the numerical simulations the loss of stability by divergence and flutter will be analyzed. It clearly appears that the piezoelectric actuation measured in terms of the feedback gain, affects the characteristic equation (25), and as a results its roots, and implicitly the stability boundaries.

8. NUMERICAL SIMULATIONS AND DISCUSSION

The numerical simulations are performed by considering the beam geometrical characteristics as $R = 5$ in (0·127 m), $L = 80$ in (2·032 m) and $h = 0{\cdot}4$ in ($1{\cdot}016 \times 10^{-2}$ m). The material of the beam is considered to be graphite-epoxy whose on-axis elastic characteristics are as follows: $E_1 = 30 \times 10^6$ psi ($20{\cdot}68 \times 10^{10}$ N/m^2), $E_2 = E_3 = 0{\cdot}75 \times 10^6$ psi ($5{\cdot}17 \times 10^9$ N/m^2), $G_{12} = 0{\cdot}45 \times 10^6$ psi ($3{\cdot}10 \times 10^9$ N/m^2), $G_{23} = G_{13} = 0{\cdot}37 \times 10^6$ psi ($2{\cdot}55 \times 10^9$ N/m^2), $\nu_{21} = \nu_{31} = 0{\cdot}00625$, $\nu_{32} = 0{\cdot}25$, $\rho = 0{\cdot}000143$ lb s^2/in^4 (15·28 kg/m^3), whereas those of piezoactuators/sensors manufactured of PZT-4 piezoceramic are supplied in reference [9]. The extensions p^a and p^s in the circumference direction of piezoactuators and piezosensors are $\pi R/4$ and $\pi R/32$ respectively.

In Figures 3–5 for ply-angle $\theta = 0,\ 60^\circ$ and 90°, respectively, pictorial representations of the variation of the fundamental natural frequency $\bar{\omega}_1(\equiv \omega_1/\hat{\omega})$ versus the spin speed $\bar{\Omega}(\equiv \Omega/\hat{\omega})$, for various feedback control gains, and for the case of the unloaded beam $(P = 0)$ are displayed. The normalized factor $\hat{\omega} = 138.85$ rad/s is the fundamental frequency of the non-spinning and unactivated beam counterpart $(\bar{K}_p = 0)$, characterized by $\theta = 0^\circ$ and $P = 0$.

For $\bar{\Omega} = 0$, i.e., in the absence of gyroscopic effects, it is seen that the system is characterized, for each θ, by a single fundamental frequency. With the increase of the ply-angle θ, an increase of the non-rotating natural frequencies is obtained. This trend is attributed to the increase of bending stiffnesses $a_{22} = a_{33}(\equiv A)$ that is associated with the increase of the ply-angle θ [5]. As soon as the rotation starts, a fact which is accompanied by the generation of gyroscopic forces, a bifurcation of natural frequencies is experienced. In other words, due the effect of the gyroscopic Coriolis force, two distinct frequency branches of free bending vibration, namely the upper and lower frequency branches are produced. The minimum spin rate at which the lowest rotating natural frequency becomes zero valued, is called the critical spinning speed, denoted as $\bar{\Omega}_{cr}$, that corresponds to the divergence instability. Throughout these results it becomes apparent that at each ply-angle there is a specific critical spinning speed and that, the minimum and maximum ones occur at $\theta = 0$ and 90° respectively. From these figures it is readily seen that while the frequencies of the upper branch increase with the increase of the whirl, the frequencies of the lower branch decrease with the increase of $\bar{\Omega}$. The minimum spin rate at which the lowest rotating natural frequency becomes zero valued is referred to as the critical spinning speed, and corresponds to the divergence instability.

The results emerging from Figures 3–5 reveal that the piezoelectric strain actuation plays a non-negligible role towards increasing the eigenfrequencies of the non-spinning beam and postponing the occurrence of the divergence whirl instability.

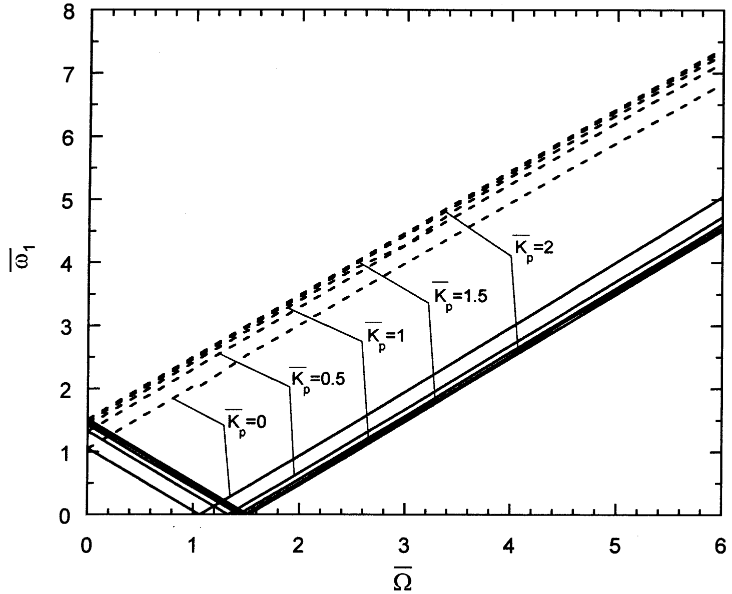

Figure 3. First natural frequencies versus spinning speed for selected values of the proportional feedback gain ($\theta = 0^\circ, \bar{P} = 0$); ——, lower branch; - - - - -, upper branch.

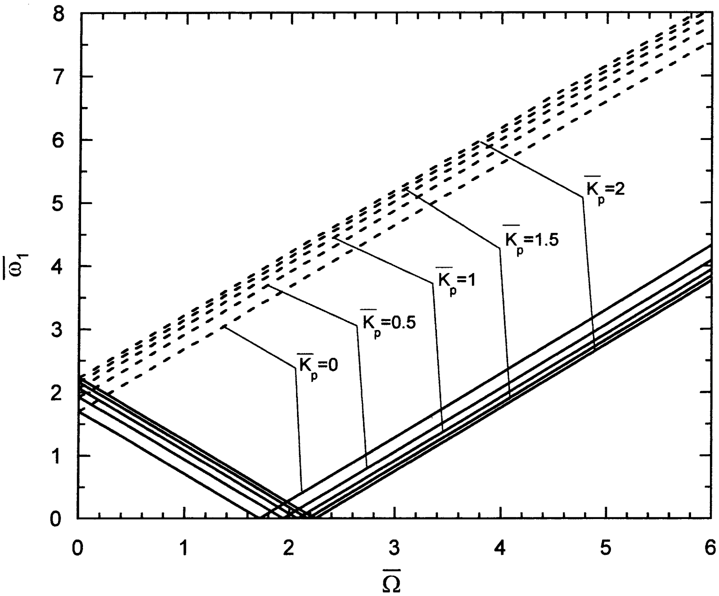

Figure 4. The counterpart of Figure 3 for the ply-angle $\theta = 60^\circ$.

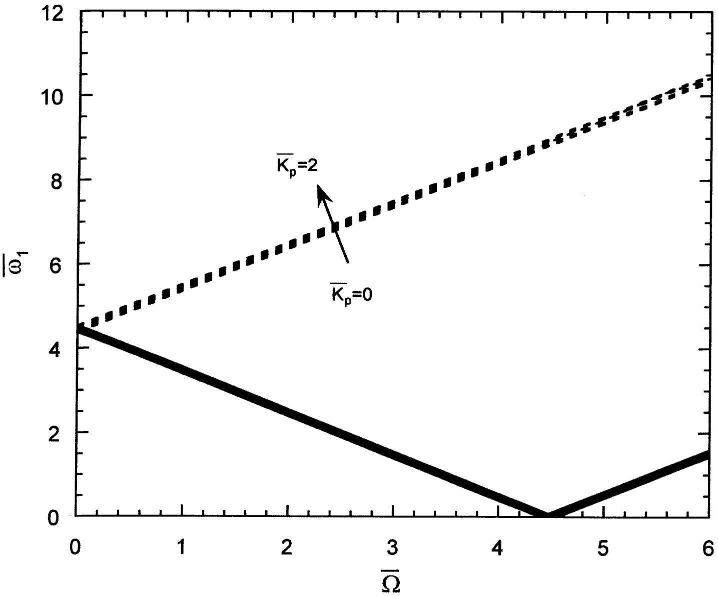

Figure 5. The counterpart of Figure 3 for the ply-angle $\theta = 90^\circ$.

At the same time it becomes apparent that the increase of the ply-angle which induces an increase of the bending stiffness [5] yields a diminision of efficiency of the control via piezoelectric strain actuation.

In Figures 6–11 there are depictions of the variation of the first and second natural frequencies, of the unloaded shaft $(\underline{P} = 0)$, as function of the feedback gain and for selected values of the spinning speed $\bar{\Omega}$. Figures 6–11 are generated for various ply-angles,

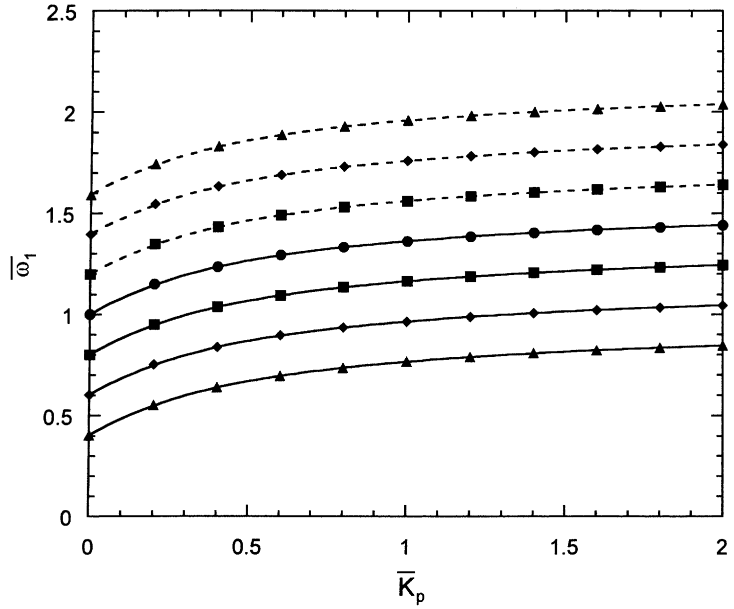

Figure 6. Upper and lower branches of the first natural frequency versus the proportional feedback gain for selected values of the spinning speed ($\theta = 0°$, $\bar{P} = 0$); ——, lower branch; – – – – –, upper branch; ●, $\bar{\Omega} = 0$; ■, $\bar{\Omega} = 0{\cdot}2$; ◆, $\bar{\Omega} = 0{\cdot}4$; ▲, $\bar{\Omega} = 0{\cdot}6$.

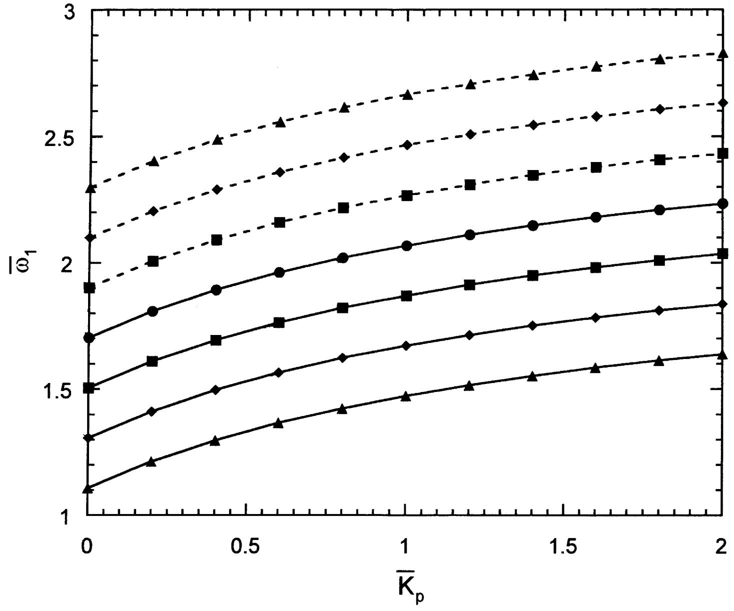

Figure 7. The counterpart of Figure 6 for $\theta = 60°$, $\bar{P} = 0$.

in the succession: $\theta = 0$, 60 and 90°. The results reveal again that for $\bar{\Omega} = 0$, there is a single bending frequency, common to flapping and lagging motions, while for $\bar{\Omega} \neq 0$, both the upper and lower frequency branches increase with the increase of the proportional feedback control gain. However, irrespective of the considered ply-angle, the second mode

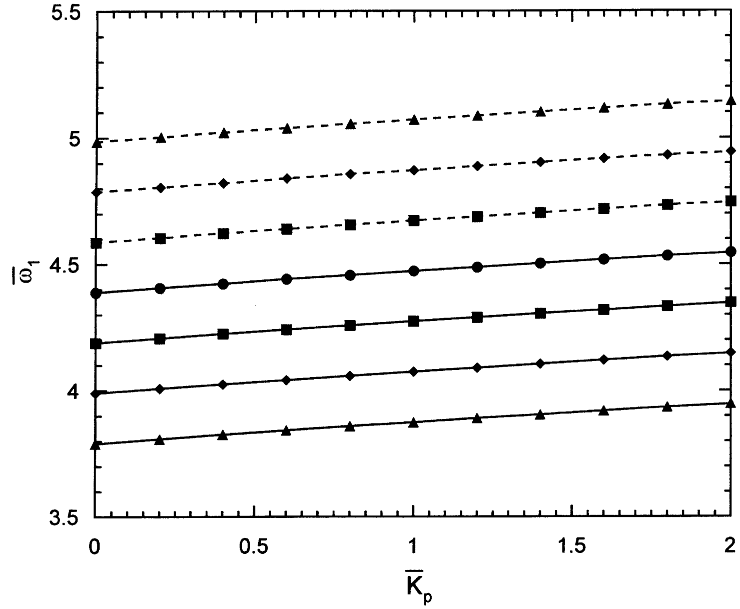

Figure 8. The counterpart of Figure 6 for $\theta = 90°$, $\bar{P} = 0$.

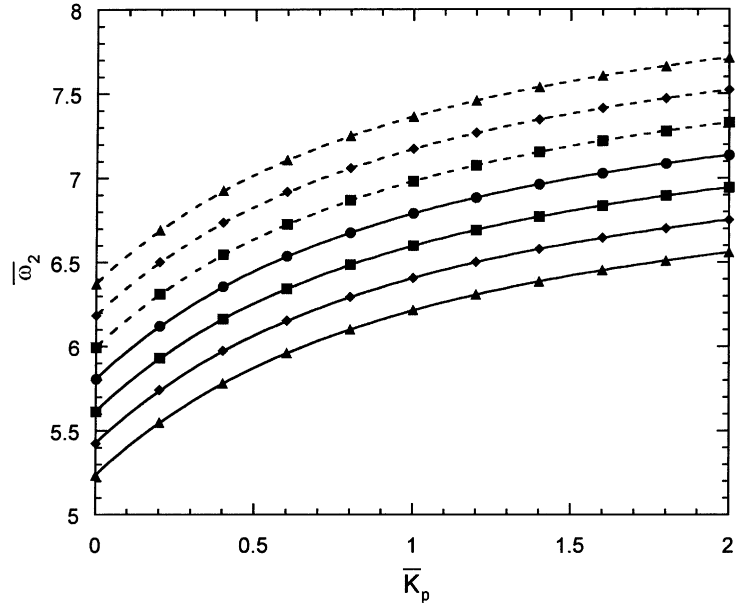

Figure 9. The counterpart of Figure 6 for the second natural frequency: ——, lower branch; — — — — —, upper branch; ●, $\bar{\Omega} = 0$; ■, $\bar{\Omega} = 0{\cdot}2$; ◆, $\bar{\Omega} = 0{\cdot}4$; ▲, $\bar{\Omega} = 0{\cdot}6$.

natural frequency features, for both the upper and lower branches, a higher increase with $\bar{K}_p$ as compared to the first mode frequencies. As concerns the whirl speed, its increase exerts on the upper and lower frequency branches a similar influence to that previously emphasized in connection with the results of Figures 3–5.

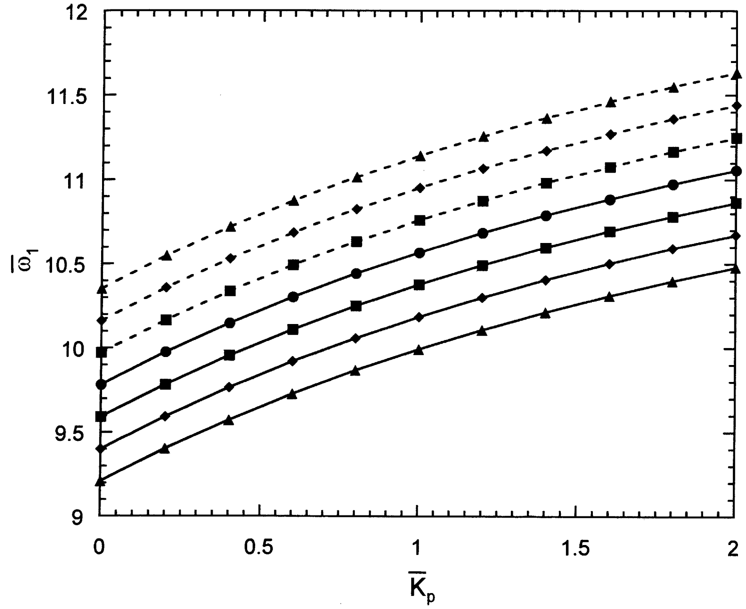

Figure 10. The counterpart of Figure 7 for the second natural frequency.

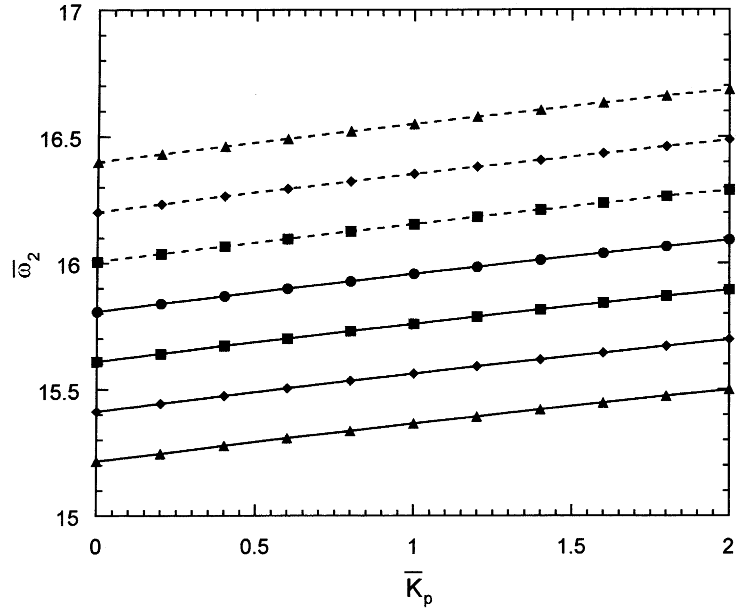

Figure 11. The counterpart of Figure 8 for the second natural frequency.

Concerning the influence of the ply-angle, its increase appears to be extremely beneficial, in the sense that in addition to the increase of non-rotating natural frequencies, it yields also an increase of frequencies belonging to both the upper and lower branches.

In Figures 12–15 there are supplied the influence of the normalized compressive axial load $\bar{P}$ and of the ply-angle on the open/closed loop first and second mode frequencies of

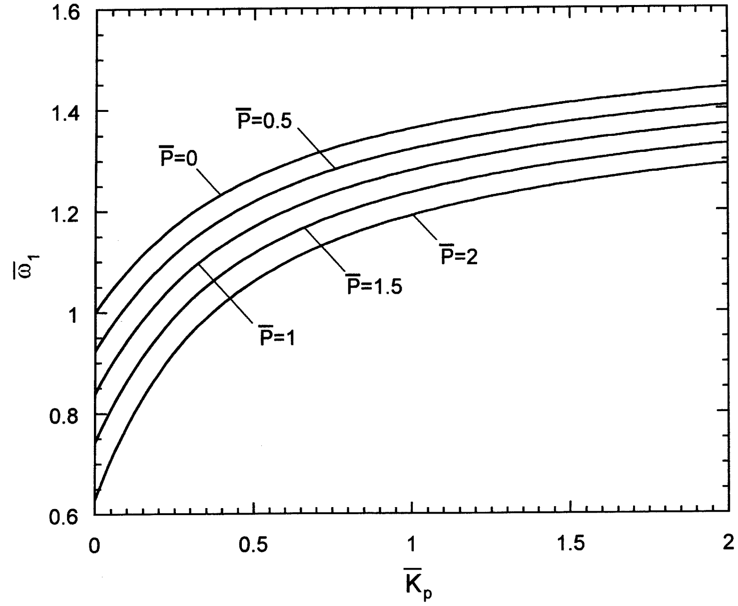

Figure 12. First non-rotating ($\bar{\Omega} = 0$) natural frequency as a function of the feedback gain, for selected values of the compressive load $\bar{P}$; $\theta = 0°$.

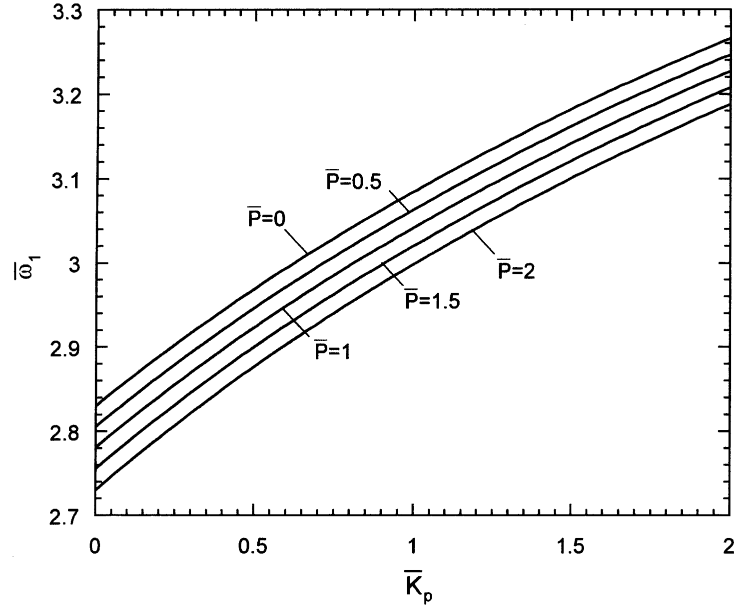

Figure 13. The counterpart of Figure 12 for $\theta = 75°$.

the non-rotating shaft. Herein, the dimensionless compressive force is defined as $\bar{P} = PL/\hat{a}_{33}$, where $\hat{a}_{33} = 1{\cdot}1787 \times 10^8$ lb in^2 is the bending normalizing stiffness corresponding to the ply-angle $\theta = 0°$.

The results reveal that: (1) the compressive load yields a decay of eigenfrequencies, (2) the piezoelectric actuation plays a substantial role towards increasing the frequencies,

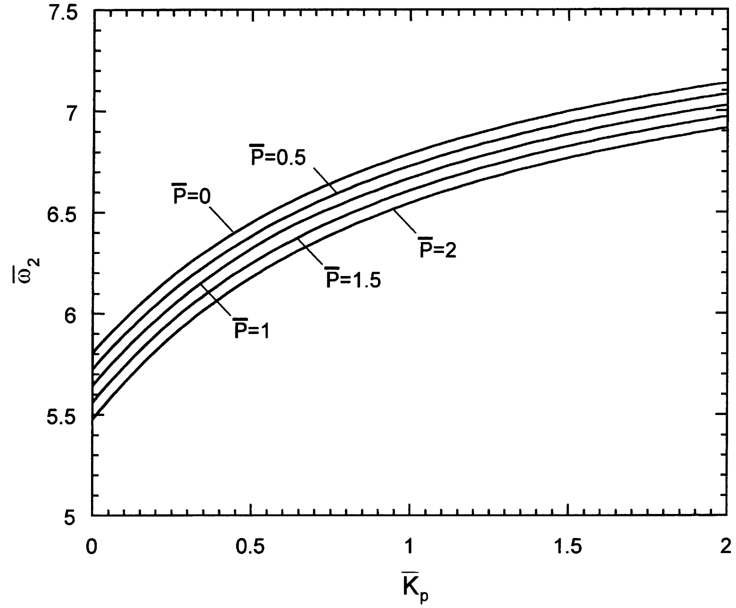

Figure 14. The counterpart of Figure 12 for the second non-rotating natural frequency.

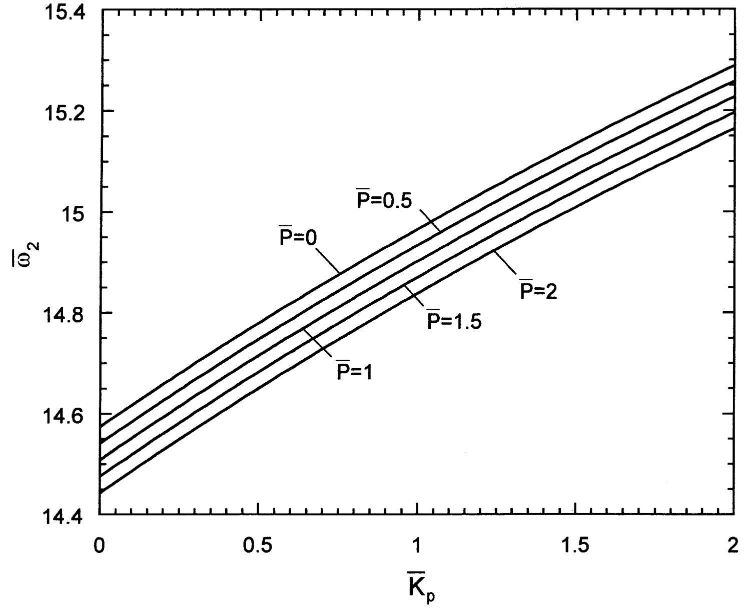

Figure 15. The counterpart of Figure 14 for $\theta = 75°$.

specially those of the first mode, and finally that (3) the increase of the ply-angle is accompanied by both a notable increase of natural frequencies and by a decay of the efficiency of the piezoelectric actuation, as well.

In Figures 16 and 17 there is depicted the variation of the first natural bending frequency of the non-rotating shaft as a function of the compressive axial load, for selected

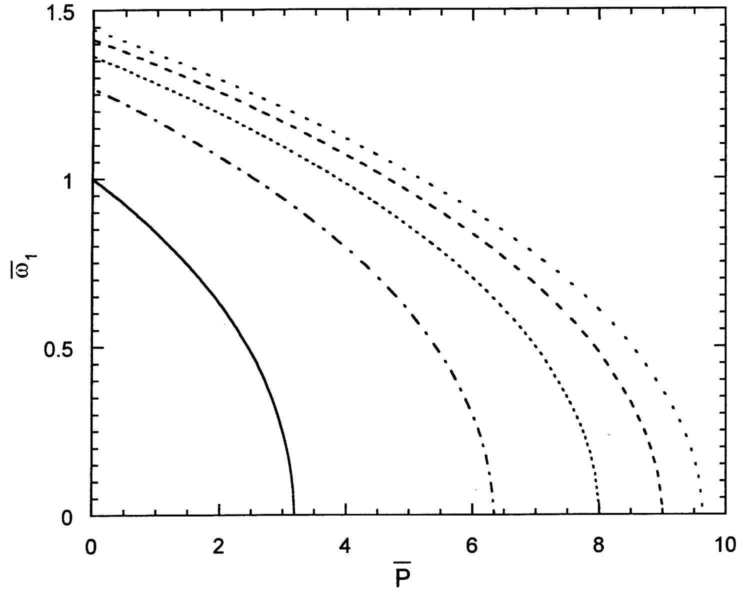

Figure 16. Variation of the first non-rotating ($\bar{\Omega} = 0$) natural frequency versus the dimensionless compressive load, for selected values of the feedback gain ($\theta = 0°$): ——, $\bar{K}_p = 0$;·—·——, $\bar{K}_p = 0{\cdot}5$; ······; $\bar{K}_p = 1$; – – – –, $\bar{K}_p = 1{\cdot}5$; ..., $\bar{K}_p = 2$.

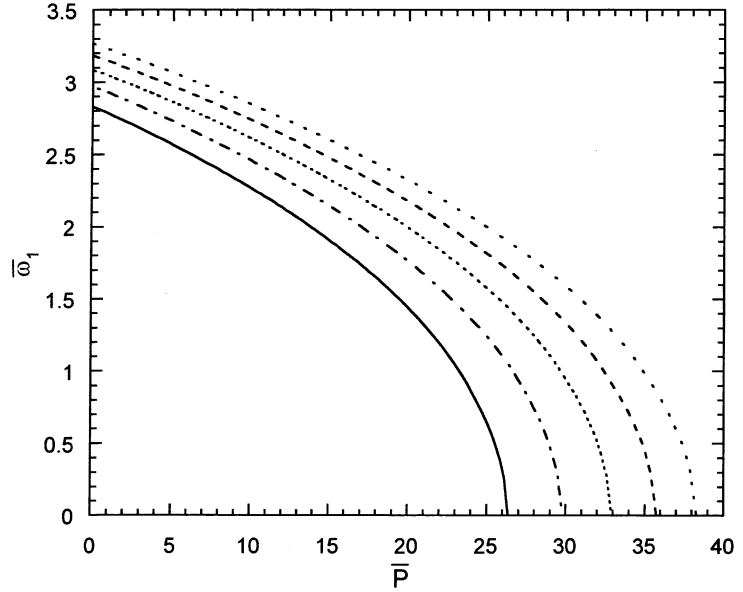

Figure 17. Counterpart of Figure 16 for $\theta = 75°$.

values of the feedback gain. These figures correspond in succession to the ply-angles $\theta = 0$ and 75° respectively. The results reveal that: (1) the increase of the compressive load yields a decrease of the natural frequency. The value of P at which the frequencies become zero valued, referred to as the buckling load, corresponds to the loss of stability by divergence; (2) the feedback actuation plays a significant role in counteracting the detrimental effect of the compressive load by increasing both the eigenfrequencies and the buckling load; (3) the increase of the ply-angle exerts a dramatic influence on both the increase of the fundamental eigenfrequency, and of the buckling load. On the other hand, the increase of the ply-angle, that is accompanied by a increase of the bending stiffness, renders more difficult the control via piezoelectric strain actuation.

In Figures 18 and 19 there are depicted the variations of the upper and lower frequency branches versus the axial compressive load, for selected values of the feedback gains and a fixed value of the spinning speed. The results of these plots reveal that for fixed values of the ply-angle and feedback gain, the divergence instability occurs at a buckling load P_{cr} for which the frequency of the lower branch becomes a zero-valued quantity.

A careful inspection of the region where the divergence occurs, reveals that in its close proximity, the increase of the compressive load yields the frequencies of the upper and lower branches to become complex conjugate. As a result, this slight increase of the compressive load, indiscernible on the plots, generates a shift of the instability from divergence to flutter. For the non-adaptive case a similar trend was reported also in reference [12], where the study was accomplished via finite element method, and very recently in reference [2].

The same plots also reveal that the increase of the ply-angle and of the feedback gain results in tremendous increases of the critical axial load. However, the same plots show that with the increase of the ply-angle, that implies an increase of the bending stiffnesses, the buckling load becomes less and less sensitive to the increase of $\bar{\Omega}$ and of the ply-angle.

Finally, in Figures 20 and 21, stability plots of the spinning system in the $\bar{\Omega}$–$\bar{P}$ plane for the ply-angles $\theta = 0$ and 45°, respectively, are displayed. In these plots S and F denote the region of stability, and flutter instability, respectively, while D denotes the divergence boundary. For $\bar{\Omega}$ and $\bar{P}$ equal to zero, $\bar{\omega}_i^2$ are real and positive and the system is stable. With the increase of $\bar{\Omega}$ and/or $\bar{P}$, instabilities by divergence or flutter may occur. Due to

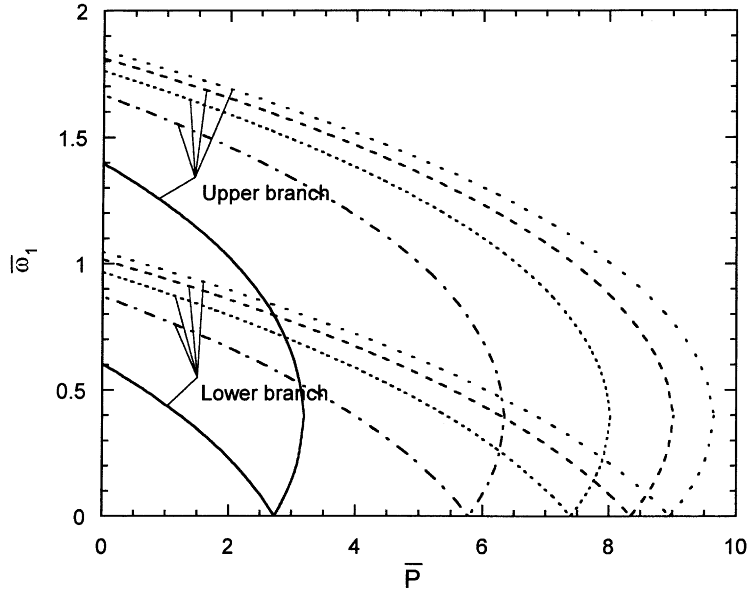

Figure 18. Variation of the upper and lower frequency branches versus the dimensionless compressive load, for selected values of the feedback gain ($\bar{\Omega} = 0{\cdot}4$, $\theta = 0°$ first natural frequency): ——, $\bar{K}_p = 0$; —·—·—, $\bar{K}_p = 0{\cdot}5$; ······; $\bar{K}_p = 1$; – – – –, $\bar{K}_p = 1{\cdot}5$; . . ., $\bar{K}_p = 2$.

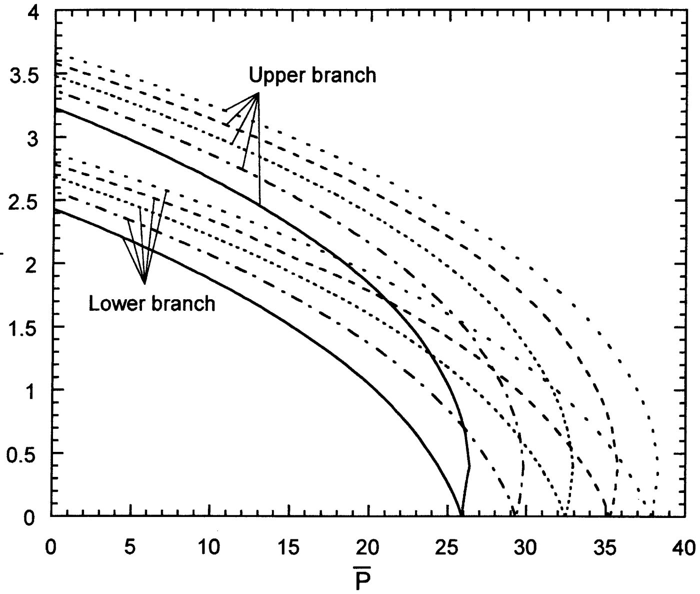

Figure 19. Counterpart of Figure 18 for $\theta = 75°$.

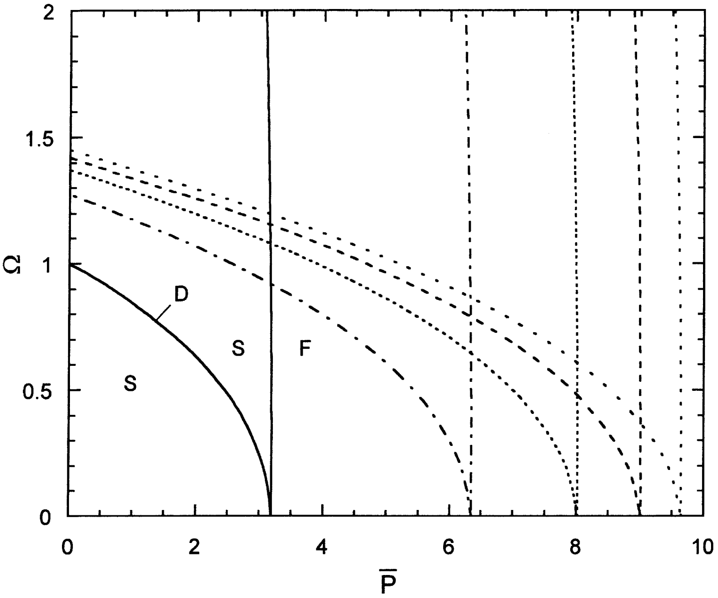

Figure 20. Stability plot in the $\bar{\Omega}$–$\bar{P}$ plane displaying the domains of stability, divergence, and flutter instability boundaries for ply-angle $\theta = 0°$ and selected values of the feedback gain: ——, $\bar{K}_p = 0$; —·——, $\bar{K}_p = 0{\cdot}5$; ······; $\bar{K}_p = 1$; – – – –, $\bar{K}_p = 1{\cdot}5$; ..., $\bar{K}_p = 2$.

the fact that the system is conservative, the initial instability will always be of divergence type, characterized by $\bar{\omega}_i^2 = 0$. The locus of such points in the plane $\bar{\Omega}$–$\bar{P}$ defines the divergence instability boundary. The plots reveal that in the plane $\bar{\Omega}$–$\bar{P}$ this instability boundary separates two stable regions, or in other words, the divergence occurs only on

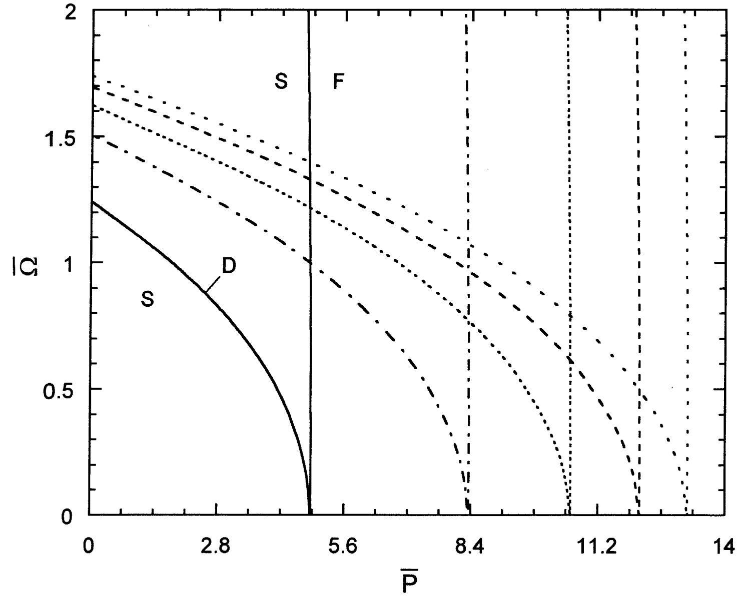

Figure 21. Counterpart of Figure 20 for $\theta = 45°$.

this boundary, without the existence of *regions* of divergence instability. Physically, this corresponds to the beam buckling in both x and y directions simultaneously, which is due to the same bending stiffness in flap and lag directions. In all these plots, the results reveal that the increase of the ply-angle yields a considerable increase of the stability domains. Similar conclusions can be formulated in connection with the implications of the piezoelectric feedback actuation. The domain of stability adjacent to the divergence instability boundary and on the right-hand side of it, reveals that the gyroscopic effects, increasing with $\bar{\Omega}$, contribute to the increase of the stability domain. On the same plots is depicted the flutter boundary corresponding to conditions involving $\bar{\Omega}$ and $\bar{P}$ yielding coalescence of the upper and lower frequency pairs. The results reveal that for specified ply-angle, the flutter boundary consists of slightly curved lines emerging at values of $\bar{P}$ slightly lower than $\bar{P}_{div}$, and at spin rates $\bar{\Omega} > 0$, where $\bar{P}_{div}$ is the buckling load obtained at $\bar{\Omega} = 0$. This result is consistent with that obtained in reference [13]. The flutter instability domain lies at the right of the curved line $\bar{P} = \bar{P}_{flutter}$ and for any $\bar{\Omega} > 0$. The results supplied in Figures 20 and 21 reveal again that the increase of ply-angle and of the feedback gain contribute to a dramatic increase of the stability domains, and to the shift of the divergence and flutter instability boundaries towards larger compressive loads. However, as is clearly seen from these plots, an increase of the ply-angle yields an unavoidable diminision of the efficiency of the piezoelectric feedback actuation.

It should be noticed that within this study the effect of material damping was not addressed. Its implications, considered in conjunction with those related to the piezoelectrically induced damping generated when the velocity feedback control is implemented, can add an additional dimension to the study carried out in this paper. This issue can be addressed by following the procedure developed in references [10, 14].

In order to have a better view of the occurrence of the instabilities, Table 1 supplies detailed information about the combined implications of the spinning speed, compressive load, ply-angle, and piezoelectric-induced actuation on both the instability by divergence and flutter of the rotating shaft, and on the domains of stability.

Table 1

Stability and instability domains as influenced by the spinning speed, compressive load, ply-angle and piezoelectric-induced actuation $(0 \leqslant \bar{P}_{stable} < \bar{P}_{div};\ \bar{P}_{div} < \bar{P}_{stable} < \bar{P}_{flutter})$

$\bar{\Omega}$	$\bar{K}_p = 0$		$\bar{K}_p = 0{\cdot}5$		$\bar{K}_p = 1$		$\bar{K}_p = 1{\cdot}5$		$\bar{K}_p = 2$	
	$\bar{P}_{div}$	$\bar{P}_{flutter}$	$\bar{P}_{div}$	$\bar{P}_{flutter}$	$\bar{P}_{div}$	$\bar{P}_{flutter}$	$\bar{P}_{div}$	$\bar{P}_{flutter}$	$\bar{P}_{div}$	$\bar{P}_{flutter}$
$\theta = 0°$										
0	3·1969	—	6·3516	—	8·0243	—	9·0114	—	9·649	—
0·4	2·726	3·1922	5·78	6·347	7·39	8·0197	8·342	9·0068	8·96	9·6444
0·8	1·23	3·1779	3·98	6·3329	5·43	8·0058	6·28	8·9929	6·84	9·6306
1·2	—	3·154	0·75	6·3095	1·952	7·9826	2·67	8·9699	3·14	9·6078
1·6	—	3·1206	—	6·2767	—	7·9502	—	8·9376	—	9·5756
2	—	3·0777	—	6·2345	—	7·9084	—	8·8962	—	9·5343
$\theta = 30°$										
0	3·57225	—	6·838	—	8·6737	—	9·798	—	10·5417	—
0·4	3·102	3·56748	6·273	6·8334	8·05	8·669	9·14	9·7934	9·86	10·5371
0·8	1·62	3·55311	4·511	6·8192	6·13	8·655	7·12	9·7795	7·77	10·5232
1·2	—	3·5293	1·37	6·7957	2·74	8·6317	3·58	9·7563	4·15	10·5001
1·6	—	3·4958	—	6·7627	—	8·599	—	9·7237	—	10·4676
2	—	3·4527	—	6·7203	—	8·5569	—	9·6819	—	10·4261
$\theta = 45°$										
0	4·8668	—	8·3573	—	10·603	—	12·1158	—	13·1833	—
0·4	4·4	4·862	7·816	8·3526	10·011	10·5983	11·49	12·1111	12·533	13·1787
0·8	2·94	4·8478	6·1422	8·3386	8·191	10·5844	9·571	12·0973	10·55	13·165
1·2	0·33	4·824	3·2	8·3151	5·01	10·5612	6·24	12·0744	7·12	13·142
1·6	—	4·7907	—	8·2824	0·29	10·5288	1·33	12·0421	2·08	13·11
2	—	4·7479	—	8·2402	—	10·487	—	12·0006	—	13·0687
$\theta = 60°$										
0	9·3139	—	13·0324	—	15·932	—	18·2177	—	20·0433	—
0·5	8·58	9·3068	12·241	13·0253	15·094	15·925	17·342	18·2109	19·14	20·0365
1	6·311	9·2853	9·801	13·0043	12·52	15·9043	14·651	18·1905	16·36	20·0162
1·5	2·3	9·2495	5·51	12·9691	8	15·8697	9·96	18·1562	11·53	19·9824
2	—	9·1993	—	12·9199	1·25	15·8212	3	18·1084	4·4	19·9351
2·5	—	9·1347	—	12·8564	—	15·7589	—	18·0469	—	19·8743
$\theta = 75°$										
0	26·3832	—	29·8243	—	32·9377	—	35·7577	—	38·3153	—
0·5	25·646	26·377	29·072	29·8183	32·172	32·9319	34·98	35·752	37·53	38·3097
1	23·41	26·3585	26·79	29·8002	29·85	32·9141	32·62	35·7346	35·14	38·2925
1·5	19·57	26·3276	22·88	29·7701	25·87	32·8846	28·58	35·7056	31·04	38·2641
2	13·97	26·2845	17·18	29·7279	20·08	32·8432	22·7	35·6649	25·1	38·2242
2·5	6·4	26·229	9·48	29·6735	12·26	32·79	14·8	35·6128	17·08	38·173
3	—	26·1611	—	29·607	2·2	32·7249	4·58	35·549	6·76	38·1103
3·5	—	26·0808	—	29·5286	—	32·6479	—	35·4735	—	38·0362
$\theta = 90°$										
0	74·2698	—	76·8045	—	79·2299	—	81·5525	—	83·7782	—
1	71·33	74·2521	73·832	76·7871	76·23	79·213	78·53	81·5359	80·724	83·7618
2	61·9	74·1989	64·31	76·7351	66·62	79·162	68·825	81·4859	70·95	83·7128
3	44·143	74·1103	46·4	76·6484	48·53	79·077	50·565	81·4026	52·51	83·6311
4	15·21	73·9861	17·2	76·5268	19·1	78·958	20·9	81·2859	22·6	83·5167
5	—	73·8263	—	76·3704	—	78·8047	—	81·1357	—	83·3694

9. CONCLUDING REMARKS

A study devoted to the vibrational and stability feedback control of spinning circular shafts modelled as thin-walled composite beams was presented. The structural model of the shaft incorporates a number of non-classical features that are essential for a reliable prediction of the vibrational response of such structural systems. Among others, the structural model includes transverse shear, rotatory inertia, anisotropy of constituent materials of the host structure, and the feedback control capability. In addition, a powerful and robust solution methodology was used to determine both the open- and closed-loop free vibrational response and stability characteristics. The strong and synergistic effects played by the directionality property of advanced composite materials and of piezoelectric actuation on vibrational response and stability boundaries of spinning shafts have been highlighted.

REFERENCES

1. O. Song and L. Librescu 1998 *Journal of Sound and Vibration* **204**, 477–494. Anisotropy and structural coupling on vibration and instability of spinning thin-walled beams.
2. O. Song, N. H. Jeong and L. Librescu 2001 *Journal of the Acoustical Society of America* **109**, 972–981. Implications of conservative and gyroscopic forces on vibration and stability of an elastically tailored rotating shaft modeled as a composite thin-walled beam.
3. Z. Qin and L. Librescu 2001 *American Institute of Aeronautics and Astronautics Journal* **39**, 2422—2424. Static and dynamic validation of a refined thin-walled composite beam model.
4. O. Song and L. Librescu 1993 *Journal of Sound and Vibration* **167**, 129–147. Free vibration of anisotropic composite thin-walled beams of closed cross-section contour.
5. L. Librescu, L. Meirovitch and O. Song 1996 *La Recherche Aerospatiale* **1**, 23–35. Refined structural modeling for enhancing vibrational and aeroelastaic characteristics of composite aircraft wings.
6. L. W. Rehfield and A. R. Atilgan 1989 *Proceedings of the First U.S.S.R.–U.S. Symposium on Mechanics of Composite Materials, Riga, Latvia, SSR*, 23–26 May, 187–196. Toward understanding the tailoring mechanisms for thin-walled composite tabular beams.
7. E. C. Smith and I. Chopra 1991 *Journal of the American Helicopter Society* **36**, Formulation and evaluation of an analytical model for composite box-beams.
8. H. S. Tzou 1993 *Piezoelectric Shells* (*Distributed Sensing and Control of Continua*). Dordrecht/Boston/London: Kluwer Academic Publication.
9. L. Librescu, O. Song and V. A. Rogers 1993 *International Journal of Engineering Science* **31**, 775–792. Adaptive vibration behavior of cantilevered structures modelled as composite thin-walled beams.
10. O. Song, J. B. Kim and L. Librescu 2001 *International Journal of Engineering Science* **39**, 71–94. Synergistic implications of tailoring and adaptive materials technology vibration control of anisotropic thin-walled beams.
11. L. Librescu, L. Meirovitch and S. S. Na 1997 *American Institute of Aeronautics and Astronautics Journal* **35**, 1309–1315. Control of cantilevers vibration via structural tailoring and Adaptive materials.
12. D. M. Ku and L. W. Chen 1994 *International Journal of Analytical and Experimental Modal Analysis* **9**, 111–123. Stability and whirl speeds of rotating shaft under axial loads.
13. K. Huseyin and R. H. Plaut 1974–1975 *Journal of Structural Mechanics* **3**, 163–177. Transverse vibrations and stability of systems with gyroscopic forces.
14. S. S. Na and L. Librescu 2001 *International Journal of Impact Engineering* **25**, 1847–1867. Dynamic response of elastically tailored adaptive cantilevers of nonuniform cross section exposed to blast pressure pulses.

APPENDIX A: STIFFNESS AND REDUCED MASS TERMS

Expressions of stiffness quantities $a_{ij}(=a_{ji})$ and reduced mass terms for cross-section circular shaft:

$$\begin{aligned}
&a_{22} = a_{33} = \pi R^2\left[K_{11} + \frac{2}{R}K_{14} + K_{44}\right] \equiv A,\\
&a_{44} = a_{55} = \pi[K_{22} + A_{44}] \equiv B,\\
&a_{25} = -a_{34} = -\pi[RK_{12} - K_{24}] \equiv S,\\
&b_4 + b_{14} = b_5 + b_{15} = \pi[m_0R^2 + m_2] \equiv C.
\end{aligned}$$

Herein,

$$\begin{aligned}
&K_{11} = A_{22} - A_{12}^2/A_{11}, \qquad K_{14} = B_{22} - \frac{A_{12}B_{12}}{A_{11}},\\
&K_{12} = A_{26} - A_{12}A_{16}/A_{11} = K_{21}, \qquad K_{44} = D_{22} = A_{66} - A_{16}^2/A_{11},\\
&K_{22} = A_{66} - A_{16}^2/A_{11}, \qquad K_{24} = B_{26} - A_{16}B_{12}/A_{11} = K_{42},
\end{aligned}$$

where A_{ij}, B_{ij} and C_{ij} denote the local stretching, coupling, and bending stiffness components respectively.

In addition, the mass terms m_0 and m_2 are expressed as

$$(m_0, m_2) = \sum_{k=1}^{N} \int_{h(k-1)}^{h_{(k)}} \rho_{(k)}(1, n^2)\,\mathrm{d}n.$$